



UNIVERSITÉ
LAVAL

Highly-elliptical-core fiber with stress-induced birefringence for mode multiplexing

Alessandro Corsi, Jun Ho Chang, Ruohui Wang, Lixian Wang, Leslie Ann Rusch and Sophie LaRochelle

OSA Optics Letters, (accepted in March 2020)

© 2020 Optical Society of America. One print or electronic copy may be made for personal use only. Systematic reproduction and distribution, duplication of any material in this paper for a fee or for commercial purposes, or modifications of the content of this paper are prohibited.

Highly-elliptical-core fiber with stress-induced birefringence for mode multiplexing

ALESSANDRO CORSI¹, JUN HO CHANG¹, RUOHUI WANG¹, LIXIAN WANG², LESLIE ANN RUSCH¹, AND SOPHIE LAROCHELLE¹

¹Centre for Optics, Photonics and Lasers (COPL), Department of Electrical and Computer Engineering, Université Laval, Canada

²Canada Research & Development, Huawei Technologies Canada Co. Ltd.

*Corresponding author: sophie.larochelle@gel.ulaval.ca

We report the polarization-maintaining properties of a highly-elliptical-core fiber surrounded by a trench that was designed to optimize the modal effective indices and bending loss for a total of five spatial modes with twofold polarization degeneracy (ten channels). In addition to the asymmetric core structure, the birefringence of the fiber is increased by the thermal stress introduced during the fabrication. We examine this effect and compare the calculated modal effective index differences to experimentally measured values. The results show a modal birefringence larger than 10^{-4} for all guided spatial modes. The fiber has a propagation loss, averaged over all mode groups, of 0.45 dB/km. The mode stability to bending is evaluated by selectively exciting/detecting each spatial mode while perturbing the fiber. This few-mode polarization-maintaining fiber is of interest for MIMO-free mode division multiplexing transmission systems.

The continuous demand for Internet traffic and cloud computing is expected to cause a capacity crunch of our current optical communications infrastructures, particularly short-reach interconnects such as data centers (DCs) [1]. Mode division multiplexing (MDM) over few-mode fibers (FMFs) is a promising technology to satisfy future data traffic demand [2]. In MDM systems, the crosstalk between the spatial modes is one of the most critical impairments to signal quality. Thus, multiple-input multiple-output (MIMO) digital signal processing (DSP) has generally been applied to undo the channel crosstalk and retrieve the information data at the receiver side. In most MDM experiment this takes the form of full-MIMO [3, 4]. In this approach, because all N spatial modes (each with two polarizations) strongly couple to each other inside the fiber or mode (de)multiplexer, MIMO processing with $2N \times 2N$ equalizer blocks is needed at the receiver side. In [3], authors used a graded-index fiber to transmit information data over 15 spatial channels with 30×30 MIMO and, more recently, 45 spatial channels with 90×90 MIMO [4]. The main drawback of this full-MIMO approach is its high complexity. Although the complexity can be relaxed to some extent by minimizing differential modal group delay, it still requires extremely heavy computational resources and power consumption.

Various design strategies of FMF have been proposed to relief the DSP burden by reducing the number of equalizer blocks [5–8]. FMF designs aim at increasing the effective index difference, Δn_{eff} , between the spatial modes or mode groups, and use only 2×2 or 4×4 MIMO equalizers to compensate the mode coupling. For example, this partial MIMO–DSP was used to exploit linearly polarized (LP) modes [5] or orbital angular momentum (OAM) modes [6]. In the former case, the authors used a step-index FMF to transmit 6 LP-mode-groups (i.e., twenty spatial channels) using two 2×2 MIMO and four 4×4 MIMO blocks, while in the latter case, a graded-index ring-core fiber was employed to transmit two modes

groups, each with 4 OAM modes (for a total of eight spatial channels), using two 4×4 MIMO blocks. The MDM transmission systems using only 2×2 MIMO blocks to manage the polarization degeneracy were also demonstrated [7]. This experiment made use of a ring-core fiber (RCF) to transmit data over two OAM modes (four channels). An optical demultiplexing technique was also utilized for data transmission over two [8] and three [9] OAM modes while avoiding the use of MIMO.

It is also possible to make the receiver MIMO-free if the polarization degeneracies of the spatial modes are lifted by an appropriate FMF design. For example, polarization-maintaining (PM) FMF designs were discussed, such as an elliptical ring-core fiber (ERCF) [10], PANDA ring-core [11] or elliptical core [12] fibers, an ERCF with an inner air hole [13] or a higher-order-mode (HOM) large effective area fibers with dual-concentric-cores and stress rods [14]. These fiber designs have in common the possibility to enhance the effective index difference between adjacent vector modes to a value higher than 10^{-4} .

In this Letter, we report the polarization-maintaining characteristics of a highly elliptical core fiber (HECF), whose geometric structure is substantially simpler than other PM-FMFs that have been proposed to date. This fiber was designed for MDM systems using 2×2 MIMO–DSP as the birefringence simulated with the geometric index profile was of the order of 10^{-5} , i.e., below the 1×10^{-4} minimum threshold for maintaining polarization [15]. In this paper, we present experimental measurements of this HECF to show that these predictions were overly pessimistic with regards to the fiber polarization maintaining properties. We incorporate the thermal stress effects in our analysis to obtain a more accurate estimate of the birefringence. The measured and simulated (with thermal stress) modal index differences are in good agreement and show a modal birefringence greater than 1×10^{-4} .

To derive the refractive index change induced by the thermal stress, we first define the stress parameters based on the fiber composition and then perform a stress analysis that takes into account the fabrication temperature. Subsequently, we use the corrected index profile to calculate the modal effective indices. Results show that stress significantly increases the effective index difference between the polarization modes, i.e., modal birefringence. We compare simulation results to the experimental measurements of effective index difference performed on the fabricated HECF through the spectral analysis of a fiber Bragg grating (FBG) response. Finally, a modal stability test confirms the possibility to exploit each spatial mode as an individual data channel.

Fig. 1(a) shows the cross-section of the designed fiber composed of a highly elliptical core surrounded by a trench to reduce the bending loss. The HECF was optimized to support five spatial modes with twofold polarization degeneracy (ten channels). More details on the HECF design can be found in [16]. The supported spatial modes have intensity profiles composed of lobes distributed as a one dimensional array and we label them as TE_{1n} and TM_{1n} , depending on the polarization state, respectively along the x -axis or the y -axis. In particular, the subscript 1 indicates the single mode operation along the short-axis (y -axis), while n is an integer indicating the number of lobes along the long-axis (x -axis).

To analyze this HECF, we consider two different sources of birefringence: the stress-induced birefringence and the geometry-induced birefringence. The first one is due to the fiber drawing and annealing process during which the fiber becomes stressed because of the different thermal expansion coefficients of the core and the cladding layers. Contrary to circularly symmetric fibers, due to the asymmetry of its core structure, the resulting stress will be different along the long-axis and the short-axis. Therefore, the isotropic glass becomes anisotropic, with a consequent change of the refractive indices along the principal axis (n_x and n_y) [17]. The second source of birefringence is related to the geometrical structure of the core, i.e., the non-circular core, and a higher core ellipticity causes a higher value of birefringence [18]. Both sources of birefringence need to be considered in the analysis of the HECF. It should be noted that the stress effect was not taken into account in previous FMFs with asymmetric structures, such as the rectangular core fiber [19, 20]. We first perform a stress analysis to determine the stress induced contribution to the core and cladding refractive index. We then calculate the modal effective indices and compare the results with and without stress-induced birefringence. The stress and modal analysis are performed by combining the Structural Model and the finite element Optical Mode Solver of COMSOL.

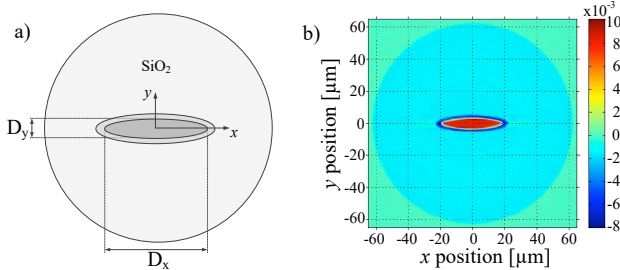


Fig. 1. (a) Cross section of the designed HECF [16], and (b) the measured index profile of fabricated HECF.

We first need to determine the material constants, such as the Young modulus E , the Poisson ratio ν , the thermal expansion coefficient α , and the material density. These constants depend on the material composition of the three different layers of the HECF: cladding, core and trench. The cladding is composed of silica (SiO_2), the core is SiO_2 doped with a 7.3% molecular fraction of germanium (GeO_2), and the trench is SiO_2 doped with a 2% molecular fraction of fluorine (F). Precise values are not available for these material constants since they are highly dependent on

the dopant concentrations. However, it is possible to estimate the values by a linear model [17, 21], which is expressed as a function of the dopant concentrations. Other constants required to perform the thermal stress analysis are the stress-optic coefficients C_1 and C_2 , the drawing temperature and the operating temperature. All values of the material constants discussed above are reported in Table 1. Note that the temperature values come from the HECF fabrication process, and the stress-optic coefficients are assumed to be the same for core, cladding and trench, i.e., equal to that of pure silica [17].

Table 1. Material constants used for the thermal stress analysis.

	SiO_2 Cladding	SiO_2 - GeO_2 Core	SiO_2 -F Trench
Young modulus E (Pa)	72.5×10^9	68.26×10^9	71.34×10^9
Poisson ratio ν	0.17	0.137	0.161
Thermal expansion coefficient α ($1/^\circ C$)	0.54×10^{-6}	0.94×10^{-6}	0.89×10^{-6}
Density (kg/m^3)	2202	2244	2180
Stress-optic coefficient C_1 (Pa^{-1})		0.69×10^{-12}	
Stress-optic coefficient C_2 (Pa^{-1})		4.19×10^{-12}	
Drawing temperature ($^\circ C$)		2215	
Operating temperature ($^\circ C$)		22	

Table 2 compares the effective index difference between the spatial modes (Δn_{eff}) and the modal birefringence (δn_{eff}) for each HECF mode [16] with and without the thermal stress analysis. A significant increase of the birefringence is observed when we take into account the thermal stress effect, as expected. At the same time, the increase of the birefringence leads to a decrease of Δn_{eff} , since the core-cladding index difference (Δn) is fixed. Nevertheless, both δn_{eff} and Δn_{eff} are above the 10^{-4} threshold, with a minimum value higher than 1.37×10^{-4} .

The HECF was fabricated in our laboratory at the COPL following a technique similar to that in [10]. The preform, with a circular core, was made with modified chemical vapor deposition (MCVD). After deposition, the cylindrical preform was cut on both sides along its length to provide two flat and parallel surfaces along its longitudinal axis. Afterwards, the preform was heated to allow surface tension and the flow of material to eliminate the flat surfaces. At the end of this process, the original circular core became elliptical [22]. The optical fiber is drawn at a temperature of $2215^\circ C$. Upon cooling, the different thermal expansion coefficients of the core and cladding result in stress components that are frozen-in the glass matrix; we refer to these as “thermal stress”. Since the preform was fabricated through MCVD, a trench surrounding the core could be introduced to reduce the bending loss, as discussed in [16]. Fig. 1(b) shows the measured refractive index profile of the fiber, which shows a good match to the design [16].

As a starting point for the HECF characterization, we used an optical time domain reflectometer (OTDR) to measure the fiber propagation loss; we found a loss of 0.45 dB/km. Note that the modal content during this measurement is unknown, so this value is an average of the propagation loss of several modes. Due to the relatively low core-cladding refractive index difference ($\Delta n = 1.1 \times 10^{-2}$), lower propagation loss was obtained compared to previously proposed MIMO-free fibers where a high Δn was used to break the degeneracy of the fiber vector modes (e.g., $\Delta n = 3 \times 10^{-2}$ [10]). Next, we characterized the effective indices of the fabricated HECF using the FBG writing technique described in [23]. A UV laser (244 nm) with a power of 60 mW and a uniform phase mask with a period Λ_{PM} equal to 1066.1 nm is used to write a 20 mm long FBG in our deuterium loaded HECF with a length of ~ 25 cm.

Table 2. Modal birefringence, δn_{eff} (shaded), and effective index difference between adjacent spatial modes, Δn_{eff} , for the designed fiber as simulated with and without thermal stress analysis, and as measured for the fabricated fiber.

	$n_{TE_{11}} - n_{TM_{11}}$	$n_{TM_{11}} - n_{TE_{12}}$	$n_{TE_{12}} - n_{TM_{12}}$	$n_{TM_{12}} - n_{TE_{13}}$	$n_{TE_{13}} - n_{TM_{13}}$	$n_{TM_{13}} - n_{TE_{14}}$	$n_{TE_{14}} - n_{TM_{14}}$	$n_{TM_{14}} - n_{TE_{15}}$	$n_{TE_{15}} - n_{TM_{15}}$
w/o thermal stress analysis	3.38×10^{-5}	1.03×10^{-3}	3.88×10^{-5}	1.27×10^{-3}	4.25×10^{-5}	1.53×10^{-3}	4.47×10^{-5}	1.8×10^{-3}	4.49×10^{-5}
w/ thermal stress analysis	1.37×10^{-4}	7.12×10^{-4}	1.41×10^{-4}	9×10^{-4}	1.45×10^{-4}	1.1×10^{-3}	1.47×10^{-4}	1.32×10^{-3}	1.49×10^{-4}
fabricated fiber	1.3×10^{-4}	8.63×10^{-4}	1.34×10^{-4}	8.97×10^{-4}	1.36×10^{-4}	1.08×10^{-3}	1.35×10^{-4}	1.18×10^{-3}	1.31×10^{-4}

Figure 2(a) shows the reflection spectrum of the FBG obtained through the use of an optical vector analyzer (OVA, Luna Technologies). The vertical dotted lines indicate the modes position for the simulated results. The peaks next to the vertical dotted lines represent the spatial modes (blue for the TE modes and red for TM modes), while the peaks in between the main peaks represent the cross-coupling between different spatial modes that can arise at wavelength positions corresponding to the mean of their Bragg wavelength peaks. Considering the large number of modes, several additional cross-coupling peaks can also be present. The strength of each peak will depend on the overlap between the two modes involved and the refractive index change, i.e., it is related to the alignment between the laser beam with respect to the elliptical core in the grating writing process. To verify that we have assigned the right spatial mode to each peak, we selectively excite one spatial mode at a time using a spatial light modulator (SLM) and image the fiber output. We then measure the transmission spectrum of the FBG to identify the Bragg wavelength of the excited mode. The experimental setup is shown in Fig. 3. An amplified spontaneous emission (ASE) source, filtered by a tunable optical bandpass filter, is incident on a SLM programmed with a first order diffraction grating that encodes the desired modes [10, 24]. This setup generates a free-space beam with the amplitude and phase distributions of the desired vector mode, facilitating the mode excitation with high coupling efficiency and mode purity. Note that the SLM diffracts light only along one polarization axis (x or y). A half-wave plate (HWP) is added to align the polarization of the free-space beam with the proper HECF axis and a 6-axis stage is used to couple the free-space beam into the HECF. SLMs provide a flexible and convenient means to generate specific mode profiles for characterization purposes but, for practical MDM systems, several other technologies could be envisioned to perform mode multiplexing and demultiplexing. These include, for example, integrated circuits in silicon photonics or free-space multi-plane light conversion [25, 26]. The detection setup for measuring the transmission spectrum of FBG is shown in Fig. 3(a). A CCD camera is used to capture the mode intensity profiles, while an optical spectrum analyzer (OSA) with a multi-mode fiber (MMF) is used to observe the transmission dip at the Bragg wavelength of the excited mode. We report, as examples, the first and fourth spatial modes in Fig. 2(b) and (c), together with the captured mode intensity profiles. By measuring the peak wavelengths, i.e., the Bragg wavelengths, we are able to extract the effective indices (n_{eff}) of the TE and TM modes, and consequently, the effective index difference between spatial and polarization modes (Δn_{eff} and δn_{eff}) (see details in [23]). In Fig. 2(a), some peaks are readily identified such as TE_{11} and TM_{11} peaks that correspond to the peaks at the longest wavelengths. In other cases, due to the presence of several cross-coupling peaks, selective modal excitation with wavelength scanning is required to identify the reflection peak of a given mode. Figure 2(b) shows the measurement for TE_{12} and TM_{12} (note that the shorter wavelength peak of this three peaks structure corresponds to cross-coupling between TM_{11} and TM_{13}).

The results, summarized in Table 2, of the measured δn_{eff} and Δn_{eff} closely match the simulated values obtained from the fiber design considering the thermal stress. In particular, the birefringence (δn_{eff}) shows values higher than 10^{-4} . We also see that Δn_{eff} slightly increases with the mode order. Both results were expected from simulations. It should be

noted that the fabricated fiber had core dimensions that were larger than the design, $36.1 \mu\text{m}$ for D_x ($31.5 \mu\text{m}$ in the design) and $7.17 \mu\text{m}$ for D_y ($6.1 \mu\text{m}$ in the design). Consequently, the fiber supports 6th order spatial modes as we can observe from the left most peaks in Fig. 2(a) and from the captured mode profile.

Subsequently, we replaced the FBG sample with a 5 m length HECF to characterize the mode profiles and stability, and polarization maintaining properties. Although the fiber is short, it was bent and twisted. We used the detection setup shown in Fig. 3(b), where a CCD camera captures the beam profiles at the HECF output and a power meter (PM) monitors the

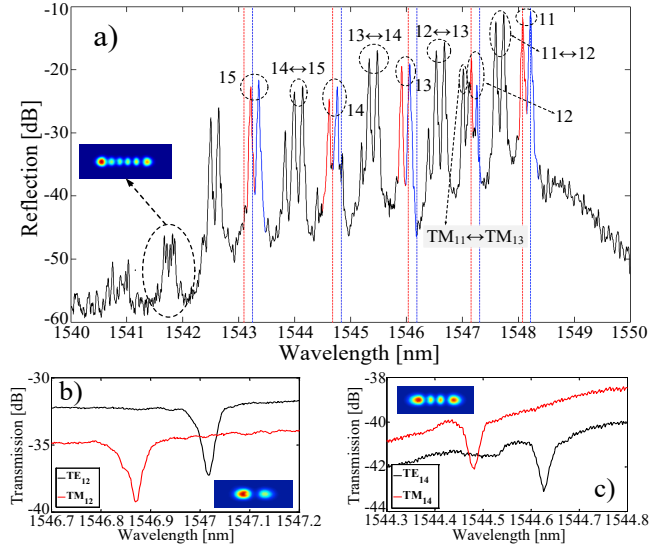
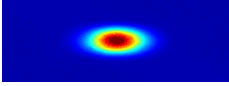
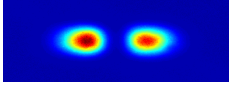
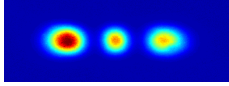
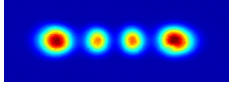
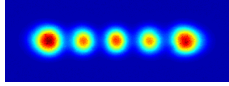


Fig. 2. (a) Measured reflection spectrum of a FBG written in the HECF. The simulated Bragg wavelengths of each spatial mode are indicated by vertical dotted lines. Peaks and line colors are blue for TE, red for TM, and black for cross-coupling between spatial modes. Transmission spectrum of (b) second order modes, TE_{12} and TM_{12} , and (c) fourth order modes, TE_{14} and TM_{14} .

output power. For alignment, we first excite the fundamental mode and adjusted the 6-axis stage so that we maximize the power at the HECF output. We then change the SLM pattern to excite the higher order fiber modes without touching the setup again. The measured intensity profiles of the five modes are displayed in Table 3.

Table 3. Observation of mode stability in a 5 meter-long HECF.

	TE ₁₁ & TM ₁₁	TE ₁₂ & TM ₁₂	TE ₁₃ & TM ₁₃	TE ₁₄ & TM ₁₄	TE ₁₅ & TM ₁₅
δn_{eff}	1.3×10^{-4}	1.34×10^{-4}	1.36×10^{-4}	1.35×10^{-4}	1.31×10^{-4}
PER	26.3 dB	25.1 dB	24.1 dB	26.3 dB	24.1 dB
ΔP	~ 0.01 dB	~ 0.03 dB	~ 0.04 dB	~ 0.13 dB	~ 0.24 dB
Mode intensity profile					

We observed the stability of the spatial modes by monitoring the mode power at the fiber output while bending the HECF along a 30 mm radius rod. Even after five turns, only small power fluctuations (ΔP) was observed, and the modes showed negligible changes in their intensity profiles. Mode coupling between the different polarization modes in a same spatial mode was also investigated by monitoring the polarization extinction ratio at the fiber output using a linear polarizer. The polarizer was rotated from 0° to 90° in order to detect the highest and the lowest powers and their ratio, which is the polarization extinction ratio (PER), was higher than 24 dB. Those results are summarized in Table 3 together with the birefringence (δn_{eff}) and the mode intensity profiles captured by the CCD camera at the fiber output. We observe clear lobes distributed as a one-dimensional array, in agreement with the intensity distribution of the simulated vector modes [16]. Since similar characteristics were found for the two polarizations of the same spatial mode, only those of one polarization are shown in Table 3.

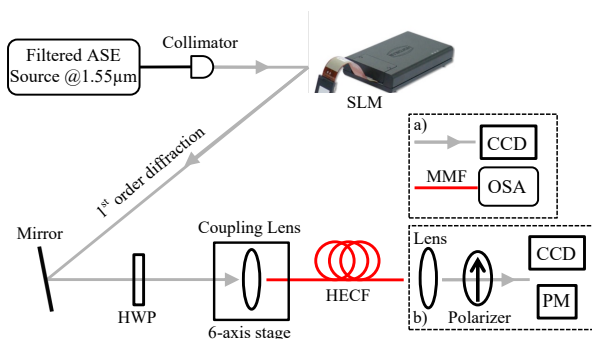


Fig. 3. Experimental setup used for the HECF characterization: (a) detection setup for observing the FBG transmission spectrum, and (b) detection setup for observing mode stability in a 5 m HECF.

In conclusion, we reported a HECF supporting five spatial modes with large stress-induced birefringence. We found that, as the core structure is highly asymmetric, the thermal stress plays an important role in the modal birefringence. By including this effect in the fiber modeling, we found good agreement between the simulated and measured effective index difference between all modes. This work demonstrates experimentally how the birefringence can reach high values by exploiting thermal-induced stress during the fiber fabrication. In this regard, the HECF showed a high effective index difference between a large number of vector modes, i.e., the minimum index difference was more than 1.3×10^{-4} between polarization modes. In addition to a large separation of the spatial modes, the modal birefringence should thus be sufficient to reduce mode coupling between polarizations and allow MIMO-free transmission over short data links.

Funding Information. This research is part of the CRC in Advanced photonic technologies for communications. It was funded by the Natural Sciences and Engineering Research Council of Canada (NSERC) and Huawei through a partnership project grant (CRDPJ 515539-17).

References

- R. J. Essiambre, G. Kramer, P. J. Winzer, G. J. Foschini, and B. Goebel, *J. Light Technol.* **28**, 662 (2010).
- P. J. Winzer, D. T. Neilson, and A. R. Chraplyvy, *Opt. Express* **26**, 24190 (2018).
- N. K. Fontaine, R. Ryf, H. Chen, A. V. Benitez, J. E. A. Lopez, R. Amezcua-Correa, *et al.*, *Optical Fiber Comm. Conference Post Deadline Papers* (Optical Society of America, 2015), paper Th5C.1.
- R. Ryf, N. K. Fontaine, S. Wittek, K. Choutagunta, M. Mazur, H. Chen, *et al.*, *2018 European Conference on Optical Communication (ECOC), Rome, 2018*, pp. 1-3.
- D. Soma, S. Beppu, Y. Wakayama, K. Igarashi, T. Tsuritani, I. Morita, and M. Suzuki, *J. Light Technol.* **36**, 1375 (2018).
- G. Zhu, Z. Hu, X. Wu, C. Du, W. Luo, Y. Chen, X. Cai, J. Liu, J. Zhu, and S. Yu, *Opt. Express* **26**, 594 (2018).
- R. M. Nejad, K. Allahverdyan, P. Vaity, S. Amiralzadeh, C. Brunet, Y. Messaddeq, S. LaRochelle, and L. A. Rusch, *J. Light Technol.* **34**, 4252 (2016).
- N. Bozinovic, Y. Yue, Y. Ren, M. Tur, P. Kristensen, H. Huang, A. E. Willner, and S. Ramachandran, *Science* **340**, 1545 (2013).
- K. Ingerslev, P. Gregg, M. Galili, F. Da Ros, H. Hu, F. Bao, M. A. U. Castaneda, P. Kristensen, A. Rubano, L. Marrucci, K. Rottwitz, T. Morioka, S. Ramachandran, and L. K. Oxenløwe, *Opt. Express* **26**, 20225 (2018).
- L. Wang, R. M. Nejad, A. Corsi, J. Lin, Y. Messaddeq, L. A. Rusch, and S. LaRochelle, *Opt. Express* **25**, 11736 (2017).
- H. Yan, S. Li, Z. Xie, X. Zheng, H. Zhang, and B. Zhou, *Photon. Res.* **5**, 1 (2017).
- S. Chen, and J. Wang, *Opt. Lett.* **43**, 3718 (2018).
- J. Zhao, M. Tang, T. Oh, Z. Feng, C. Zhao, R. Liao, S. Fu, P. P. Shum, and D. Liu, *Photon. Res.* **5**, 261 (2017).
- R. Ahmad, M. F. Yan, J. W. Nicholson, K. S. Abedin, P. S. Westbrook, C. Headley, P. W. Wisk, E. M. Monberg, and D. J. DiGiovanni, *Opt. Lett.* **42**, 2591 (2017).
- P. Gregg, P. Kristensen, and S. Ramachandran, *Opt. Express* **24**, 18938 (2016).
- A. Corsi, J. H. Chang, L. A. Rusch, and S. LaRochelle, *IEEE Photonic Journal* **11**, (2019).
- W. Urbanczyk, T. Martynkien, and W. J. Bock, *Appl. Optics* **40**, 1911 (2001).
- G. Milione, E. Ip, P. Ji, Y. K. Huang, T. Wang, M. J. Li, J. Stone, and G. Peng, *Opt. Fiber Comm. Conf.* (Optical Society of America, 2017), paper Tu2.1.
- L. Rechtman, and D. M. Marom, *Optical Fiber Comm. Conference* (Optical Society of America, 2017), paper Th2A.10.
- L. Rechtman, D. M. Marom, J. S. Stone, G. Peng, and M.-J. Li, *IEEE Photonics Conference (IPC, 2017)*, pp. 43-44.
- R. Guan, F. Zhu, Z. Gan, D. Huang, and S. Liu, *Opt. Fiber Technol.* **11**, 240 (2005).
- R. H. Stolen, V. Ramaswamy, P. Kaiser, and W. Pleibel, *Appl. Phys. Lett.* **33**, 699, (1978).
- L. Wang, P. Vaity, B. Ung, Y. Messaddeq, L. A. Rusch, and S. LaRochelle, *Opt. Express* **22**, 15653 (2014).
- A. Corsi, L. Wang, L. A. Rusch, and S. LaRochelle, *IEEE Photon. Technol. Lett.* **30**, 581 (2018).
- C. Li, D. Liu, and D. Dai, *Nanophotonics* **8**, 227, (2019).
- N. Barre, B. Denolle, P. Jian, J. Morizur, and G. Labroille, *Optical Fiber Comm. Conference* (Optical Society of America, 2017), paper Th2A.7.

FULL REFERENCES

1. R. J. Essiambre, G. Kramer, P. J. Winzer, G. J. Foschini, and B. Goebel, "Capacity Limits of Optical Fiber Networks", *J. Lightwave Technol.* **28**(4), 662-701 (2010).
2. P. J. Winzer, D. T. Neilson, and A. R. Chraplyvy, "Fiber-optic transmission and networking: the previous 20 and the next 20 years [Invited]", *Opt. Express* **26**(8), 24190-24239 (2018).
3. N. K. Fontaine, R. Ryf, H. Chen, A. V. Benitez, J. E. A. Lopez, R. Amezcua-Correa, B. Guan, B. Ercan, R. P. Scott, S. J. B. Yoo, L. Grüner-Nielse, Y. Sun, and R. J. Lingle, "30x30 MIMO Transmission over 15 Spatial Modes", *Optical Fiber Communication Conference Post Deadline Papers* (Optical Society of America, 2015), paper Th5C.1.
4. R. Ryf, N. K. Fontaine, S. Wittek, K. Choutagunta, M. Mazur, H. Chen, J. C. Alvarado-Zacarias, R. Amezcua-Correa, M. Capuzzo, R. Kopf, A. Tate, H. Safar, C. Bolle, D. T. Neilson, E. Burrows, K. Kim, M. Bigot-Astruc, F. Achten, P. Sillard, A. Amezcua-Correa, J. M. Kahn, J. Schröder, and J. Carpenter, "High-Spectral-Efficiency Mode-Multiplexed Transmission over Graded-Index Multimode Fiber", *European Conference on Optical Communication Post Deadline Papers* (2018).
5. D. Soma, S. Beppu, Y. Wakayama, K. Igarashi, T. Tsuritani, I. Morita, and M. Suzuki, "257-Tbit/s Weakly Coupled 10-Mode C + L-Band WDM Transmission", *J. Lightwave Technol.* **36**(6), 1375-1381 (2018).
6. G. Zhu, Z. Hu, X. Wu, C. Du, W. Luo, Y. Chen, X. Cai, J. Liu, J. Zhu, and S. Yu, "Scalable mode division multiplexed transmission over a 10-km ring-core fiber using high-order orbital angular momentum modes", *Opt. Express* **26**(2), 594-604 (2018).
7. R. M. Nejad, K. Allahverdyan, P. Vaity, S. Amiralzadeh, C. Brunet, Y. Messaddeq, S. LaRochelle, and L. A. Rusch, "Mode Division Multiplexing Using Orbital Angular Momentum Modes Over 1.4-km Ring Core Fiber", *J. Lightwave Technol.* **34**(18), 4252-4258 (2016).
8. N. Bozinovic, Y. Yue, Y. Ren, M. Tur, P. Kristensen, H. Huang, A. E. Willner, and S. Ramachandran, "Terabit-Scale Orbital Angular Momentum Mode Division Multiplexing in Fibers", *Science* **340**(6140), 1545-1548 (2013).
9. K. Ingerslev, P. Gregg, M. Galili, F. Da Ros, H. Hu, F. Bao, M. A. U. Castaneda, P. Kristensen, A. Rubano, L. Marrucci, K. Rottwitz, T. Morioka, S. Ramachandran, and L. K. Oxenløwe, "12 mode, WDM, MIMO-free orbital angular momentum transmission", *Opt. Express* **26**(16), 20225-20232 (2018).
10. L. Wang, R. M. Nejad, A. Corsi, J. Lin, Y. Messaddeq, L. A. Rusch, and S. LaRochelle, "Linearly polarized vector modes: enabling MIMO-free mode-division multiplexing", *Opt. Express* **25**(10), 11736-11748 (2017).
11. H. Yan, S. Li, Z. Xie, X. Zheng, H. Zhang, and B. Zhou, "Design of PANDA ring-core fiber with 10 polarization-maintaining modes", *Photon. Res.* **5**(1), 1-5 (2017).
12. S. Chen, and J. Wang, "Design of PANDA-type elliptical-core multimode fiber supporting 24 fully lifted eigenmodes", *Opt. Lett.* **43**(15), 3718-3721 (2018).
13. J. Zhao, M. Tang, T. Oh, Z. Feng, C. Zhao, R. Liao, S. Fu, P. P. Shum, and D. Liu, "Polarization-maintaining few mode fiber composed of a central circular-hole and an elliptical-ring core", *Photon. Res.* **5**(3), 261-266 (2017).
14. R. Ahmad, M. F. Yan, J. W. Nicholson, K. S. Abedin, P. S. Westbrook, C. Headley, P. W. Wisk, E. M. Monberg, and D. J. DiGiovanni, "Polarization-maintaining, large-effective-area, higher-order-mode fiber," *Opt. Lett.* **42**(13), 2591-2594 (2017).
15. P. Gregg, P. Kristensen, and S. Ramachandran, "13.4km OAM state propagation by recirculating fiber loop", *Opt. Express* **24**(17), 18938-18947 (2016).
16. A. Corsi, J. H. Chang, L. A. Rusch, and S. LaRochelle, "Design of Highly Elliptical Core Ten-Mode Fiber for Space Division Multiplexing With 2x2 MIMO", *IEEE Photonics Journal* **11**(2), (2019).
17. W. Urbanczyk, T. Martynkien, and W. J. Bock, "Dispersion effects in elliptical-core highly birefringent fibers", *Appl. Optics* **40**(12), 1911-1920 (2001).
18. G. Milione, E. Ip, P. Ji, Y. K. Huang, T. Wang, M. J. Li, J. Stone, and G. Peng, "MIMO-less Space Division Multiplexing with Elliptical Core Optical Fibers", *Optical Fiber Communication Conference* (Optical Society of America, 2017), paper Tu2J.1.
19. L. Rechtman, and D. M. Marom, "Rectangular versus circular fiber core designs: New opportunities for mode division multiplexing?", *Optical Fiber Communication Conference* (Optical Society of America, 2017), paper Th2A.10.
20. L. Rechtman, D. M. Marom, J. S. Stone, G. Peng, and M.-J. Li, "Mode characterization of rectangular core fiber", *IEEE Photonics Conference (IPC, 2017)*, pp. 43-44.
21. R. Guan, F. Zhu, Z. Gan, D. Huang, and S. Liu, "Stress birefringence analysis of polarization maintaining optical fibers", *Opt. Fiber Technol.* **11**, 240-254 (2005).
22. R. H. Stolen, V. Ramaswamy, P. Kaiser, and W. Pleibel, "Linear polarization in birefringent single-mode fibers", *Appl. Phys. Lett.*, **33**(8), 699-701, (1978).
23. L. Wang, P. Vaity, B. Ung, Y. Messaddeq, L. A. Rusch, and S. LaRochelle, "Characterization of OAM fibers using fiber Bragg gratings", *Opt. Express* **22**(13), 15653-15661 (2014).
24. A. Corsi, L. Wang, L. A. Rusch, and S. LaRochelle, "Mode Loss Measurement in Few-Mode Fibers With a Microwave Interferometric Technique", *IEEE Photon. Technol. Lett.* **30**(6), 581-584 (2018).
25. C. Li, D. Liu, and D. Dai, "Multimode silicon photonics", *Nanophotonics* **8**, 227-247, (2019).
26. N. Barre, B. Denolle, P. Jian, J. Morizur, and G. Labroille, "Broadband, mode selective 15-mode multiplexer based on multi-plane light conversion", *Optical Fiber Communication Conference* (Optical Society of America, 2017), paper Th2A.7.